Carbon 173 (2021) 968–979

Contents lists available at ScienceDirect

Carbon

journal homepage: www.elsevier.com/locate/carbon

Research Article

# Effect of pore geometry on ultra-densified hydrogen in microporous carbons

Mi Tian [a, b, *], Matthew J. Lennox [b], Alexander J. O'Malley [c], Alexander J. Porter [c], Benjamin Krüner [d, e], Svemir Rudić [f], Timothy J. Mays [b], Tina Düren [b], Volker Presser [d, e], Lui R. Terry [g], Stephane Rols [h], Yanan Fang [i], Zhili Dong [i], Sebastien Rochat [j], Valeska P. Ting [g, **]

[a] College of Engineering, Mathematics, and Physical Sciences, University of Exeter, Exeter, EX4 4QF, United Kingdom
[b] Centre for Advanced Separations Engineering, Department of Chemical Engineering, University of Bath, Bath, BA2 7AY, United Kingdom
[c] Department of Chemistry, University of Bath, Bath, BA2 7AY, United Kingdom
[d] INM - Leibniz Institute for New Materials, Campus D2 2, 66123, Saarbrücken, Germany
[e] Department of Materials Science and Engineering, Saarland University, 66123, Saarbrücken, Germany
[f] ISIS Facility, STFC, Rutherford Appleton Laboratory, Didcot, OX11 0QX, United Kingdom
[g] Department of Mechanical Engineering, University of Bristol, Bristol, BS8 1TR, United Kingdom
[h] Institute Laue-Langevin, Grenoble Cedex 9, Grenoble, France
[i] School of Materials Science and Engineering, Nanyang Technological University, Singapore
[j] School of Chemistry, Bristol Composites Institute and Department of Engineering Mathematics, University of Bristol BS8 1TR, United Kingdom

ARTICLE INFO

*Article history:*
Received 7 October 2020
Received in revised form
16 November 2020
Accepted 19 November 2020
Available online 23 November 2020

*Keywords:*
Microporous carbon
Hydrogen storage
Confinement
High-pressure adsorption
Inelastic neutron scattering
Molecular dynamic simulation

ABSTRACT

Our investigations into molecular hydrogen ($H_2$) confined in microporous carbons with different pore geometries at 77 K have provided detailed information on effects of pore shape on densification of confined $H_2$ at pressures up to 15 MPa. We selected three materials: a disordered, phenolic resin-based activated carbon, a graphitic carbon with slit-shaped pores (titanium carbide-derived carbon), and single-walled carbon nanotubes, all with comparable pore sizes of <1 nm. We show *via* a combination of *in situ* inelastic neutron scattering studies, high-pressure $H_2$ adsorption measurements, and molecular modelling that both slit-shaped and cylindrical pores with a diameter of ~0.7 nm lead to significant $H_2$ densification compared to bulk hydrogen under the same conditions, with only subtle differences in hydrogen packing (and hence density) due to geometric constraints. While pore geometry may play some part in influencing the diffusion kinetics and packing arrangement of hydrogen molecules in pores, pore size remains the critical factor determining hydrogen storage capacities. This confirmation of the effects of pore geometry and pore size on the confinement of molecules is essential in understanding and guiding the development and scale-up of porous adsorbents that are tailored for maximising $H_2$ storage capacities, in particular for sustainable energy applications.



## 1. Introduction

Molecular hydrogen ($H_2$) has received much attention as a potentially sustainable, zero-carbon energy vector due to its global abundance in the form of water and biomass, its relative ease of production, for example via water electrolysis or thermochemical treatment of biomass, and the fact that it produces only water upon complete oxidation. While $H_2$ has the highest gravimetric energy density of any chemical fuel (with a higher heating value of 142 MJ $kg^{-1}$), it exists as a very low-density gas under ambient conditions (~0.08 kg $m^{-3}$) leading to relatively low volumetric energy density compared with liquid fuels. Hence gaseous $H_2$ must be densified to be stored and transferred effectively, which has proven to be technically challenging. An alternative to pressurising or liquefying $H_2$ to increase its volumetric energy density is the physisorption of $H_2$ in microporous materials such as activated carbons [1–4], zeolites, metal-organic frameworks [5] and certain

* Corresponding author. College of Engineering, Mathematics, and Physical Sciences, University of Exeter, Exeter, EX4 4QF, United Kingdom.
** Corresponding author.
*E-mail addresses:* m.tian@exeter.ac.uk (M. Tian), v.ting@bristol.ac.uk (V.P. Ting).

https://doi.org/10.1016/j.carbon.2020.11.063

porous polymers [6–8]. These microporous materials (with pore diameter < 2 nm) can spontaneously adsorb and compress hydrogen within their pores, allowing the hydrogen to be stored at much higher densities than in high-pressure tanks (which typically store hydrogen at pressures of 35–70 MPa) [6] and at significantly higher temperatures than storage as liquefied $H_2$ (20 K).

This density enhancement is the result of molecular confinement within the micropores of the materials. Confinement has been shown to have a strong effect on the packing and phase behaviour of confined phases [9]. The impact of pore geometries on hydrogen densification and the mechanisms of densification are not well understood, although a very recent study reported that sub-nanometre pores of spherical and cylindrical shape strongly limit the diffusion of $H_2$ [10]. Moreover, many studies of water within the pores of carbon nanomaterials have indicated stabilisation of states of matter not normally present at such pressures or temperatures, which can be attributed to enhancement or disruption of the hydrogen bonding network under confinement. Erko et al. reported that water confined in 2 nm diameter cylindrical pores of silica undergoes considerable structural changes from low-density amorphous ice to high-density crystalline ice with decreasing pore size [11], with Raman measurements suggesting the existence of both a non-freezable wall layer and a different hydrogen-bonded core water phase. Experimental studies on water encapsulated in carbon nanotubes have also demonstrated a transformation from a liquid-like state to ordered tubular or helical ice structures called "ice nanotubes" [12–14]. Confinement can also lead to elevation or depression of freezing points due to interactions of the adsorbed fluid with the pore surfaces. X-ray diffraction studies of ice nanotubes inside single-walled carbon nanotubes (SWCNTs) show that the melting/freezing temperature of ice nanotubes increases with decreasing SWCNT diameter [15]. Choi et al. found the optimum microporous structures and uniform particle morphology enabling efficient methane ($CH_4$) molecular packing in micropores [16]. In the case of hydrogen, confinement in porous Vycor glass with the mean pore diameter of ~6 nm has been shown to prompt liquefaction at temperatures above the triple point of bulk $H_2$ [17], while the freezing transition temperatures of $H_2$ and molecular deuterium ($D_2$) confined inside a range of porous aerogels were shown to be lower [9,18] compared to the bulk gas. Each of these deviations from the classical phase behaviours of the bulk properties observed for fluids in tight confinement is a result of the combination of interactions between the fluids and the walls and geometrical or steric limitations, and thus hydrogen densification and phase behaviours are expected to be heavily dependent on the size and shape of the confining space.

In microporous hydrogen storage materials, molecular confinement involves van der Waals interactions between the adsorbed $H_2$ and the pore surface, and is amplified for small pores due to overlapping potentials from opposing pore walls. The role of pore diameter in increasing the density of confined hydrogen has been well-studied. For example, Gogotsi et al. showed for carbide-derived carbons (CDCs) with an accurately controlled pore size, that the materials with the smallest pore sizes (of diameter 0.6–0.7 nm) provide the largest $H_2$ uptake per unit specific surface area (SSA) at 77 K, whereas pores larger than ~1.5 nm in diameter contributed little to hydrogen storage [2,19,20]. From these studies [2,21], the average density of hydrogen in CDCs with a micropore size below 0.7 nm at 0.1 MPa was estimated to be close to the density of liquid hydrogen [21]. Our recent neutron scattering studies of hydrogen adsorbed in activated carbon with a pore diameter of ~0.7 nm found limiting hydrogen densities in the region of 100 kg $m^{-3}$ at 77 K [22], suggestive of solid hydrogen densities at temperatures and pressures where this would not be classically possible in bulk $H_2$. This high hydrogen density (larger than the ~76 kg $m^{-3}$ density of bulk liquid hydrogen at the critical point) in slit-shaped micropores of pore size < 1 nm at 77 K has recently been investigated by Rogacka et al. through Monte Carlo simulations [23]. These authors simulated hydrogen adsorption in carbon slit-shaped nanopores at 77 K and showed the density of the adsorbed hydrogen layer (95 kg $m^{-3}$ at 77 K) was far higher than the density of bulk liquid hydrogen at the critical point.

While the role of pore size in causing $H_2$ densification *via* confinement in microporous materials has previously been identified, the role of pore geometry on the $H_2$ densification has remained unclear. Computer simulations [24–27], such as Grand Canonical Monte Carlo (GCMC) [24,25] and density functional theory (DFT) [28], have provided molecular-level insight into the gas adsorption/desorption process, and indicated the importance of pore geometry as well as of pore size for gas sorption in nanopores. For example, Raghavan et al. [29] studied the behaviour of $H_2$ and $CH_4$ flowing through various pore geometries using a molecular dynamics approach, showing the gas permeance and adsorption layer were heavily influenced by pore geometry.

However, due to the challenges associated with experimentally probing the behaviour of light gases such as hydrogen within porous solids and challenges in using classical simulations to accurately describe quantum effects (especially at high densities and low temperature), there has been little systematic investigation into how different pore geometries affect hydrogen adsorption and densification at supercritical conditions. In the present work, we employed *in situ* neutron scattering approaches in parallel with high-pressure gas adsorption measurements further complemented by theoretical adsorption modelling and classical molecular simulations to evaluate the behaviour of adsorbed $H_2$ gas in selected pore geometries at 77 K (a temperature that is practically relevant for adsorptive $H_2$ storage applications).

Three carbon-based materials with different pore geometries were investigated using this compelling combination of experimental and computational techniques. The in-depth studies presented here provide us with insight into how differences in molecular packing of the $H_2$ confined in slit-shaped and cylindrical pores influences the efficiency of hydrogen densification.

## 2. Methods

TE7 carbon beads (sourced from MAST Carbon International) were produced from a carbonised phenolic resin-based material activated at high temperature (1173 K) in a carbon dioxide atmosphere. The TiC-CDC-800 sample was synthesised by chlorination of a TiC precursor at 1073 K, followed by annealing in hydrogen at 873 K. Single-walled carbon nanotubes (90% purity, 0.7–1.1 nm diameter) were purchased from Sigma Aldrich (Product no. is 704,121). This sample was manufactured by SouthWest Nano Technologies Inc. using patented CoMoCAT™ synthesis technology. The as-sourced SWCNTs were treated at 673 K for 40 min within 100 mL $min^{-1}$ $CO_2$ gas flow for the removal of end-caps before use.

$N_2$ isotherms were measured at 77 K with a Micromeritics 3Flex surface area and porosity analyser (Micromeritics Instrument Corporation). The samples were outgassed at 473 K for 8 h under dynamic high vacuum (~$10^{-4}$ Pa) prior to measurement. The BET surface areas were calculated in pressure ranges determined based on the consistency criteria recommended by Rouquerol et al. [30] The pore size distribution was calculated from the full $N_2$ isotherm based on the non-local density functional theory (2D-NLDFT) method [64].

The carbon powder samples for TEM observation were manually ground under ethanol in an agate mortar and then dispersed in an ultrasonic bath for 10 min. A drop of the suspension was deposited on a carbon-coated copper grid. The TEM images were collected

using a JEOL-2010 microscope with an accelerating voltage at 200 kV.

Ti content in TiC-CDC-800 was determined by thermogravimetric analysis (TGA), using a Setaram TGA analyser. About 15 mg of sample material was loaded into an alumina crucible and then heated from 293 to 1023 K at a rate of 5 K $min^{-1}$ under air at 0.15 MPa.

The Raman spectra were recorded using a Renishaw spectrometer with Ar laser excitation (514 nm) equipped with a CCD detector. All measurements were performed at room temperature.

High-pressure hydrogen adsorption/desorption measurements were measured on a Hiden Isochema HTP-1 Sieverts-type volumetric gas sorption analyser with ultra-high purity hydrogen provided by Air Products BIP-Plus (99.99996%) at 77 K using a liquid nitrogen bath for temperature control. Prior to each isothermal measurement, the ~100 mg samples were degassed *ex-situ* at 473 K for 10 h under dynamic high vacuum (~$10^{-4}$ Pa) to remove moisture and any impurities absorbed to the surface. All isotherms were fully reversible, and repeat isotherms for different samples were reproducible to within 0.3% of measured amounts absorbed.

The inelastic neutron scattering (INS) spectra of hydrogen adsorption on the TE7, TiC-CDC-800 and SWCNTs were collected on the TOSCA beamline at the Rutherford Appleton Laboratory in the UK. TOSCA is an indirect geometry spectrometer with only one value of Q ($Å^{-1}$) for each energy transfer $E_T$ ($cm^{-1}$) ($Q^2 \sim E_T/16$), has an energy window from −3 meV to + 500 meV and an excellent energy resolution in the accessible energy transfer range ($\Delta E/E_0$ ~ 1.5%) [31,32].

For the INS experiments, the carbon samples were degassed via heating ex-situ at 473 K for over 10 h under high vacuum and were then loaded in an Ar glove box into a high-pressure stainless-steel sample can. The temperature was controlled by a standard cryofurnace ancillary. The background scans of the degassed samples under dynamic vacuum at 77 K were collected (for approximately 4 h each) before the hydrogen dosing. The background scans were later subtracted from the INS spectra to correct for the presence of terminal H atoms in the sample.

Comparative INS spectra of the SWCNTs were also collected on the IN4 high-flux time-of-flight spectrometer at the Institute Laue-Langevin (ILL) in France, which has an energy window up to ~30 meV with a good resolution of 200 μeV and high flux. The SWCNTs were degassed in a vacuum oven at 473 K over 10 h, then immediately loaded into a high-pressure sample vessel. The sample vessel was attached to a Hiden HTP-1 for $H_2$ pressure control. The temperature was controlled by a cryostat *in-situ*. The background scans of the degassed SWCNTs under dynamic vacuum at 77 K were collected before the hydrogen dosing. The background scans were later subtracted from the INS spectra to correct for the presence of terminal H atoms in the sample. The INS data were collected at 77 K with $H_2$ dosing pressure at 0.1 MPa, 0.3 MPa, and 2 MPa.

The entire inelastic region (from 2 meV to 500 meV), the elastic peak (from −2 meV to 2 meV), and the rotor peak at 14.7 meV were fitted using a Gaussian function to calculate the integrated intensity and the full-width at half-maximum (FWHM).

Grand Canonical and NVT Monte Carlo (MC) simulations of $H_2$ adsorption at 77 K and pressures ranging from 0.1 Pa to 26 MPa were carried out using the MuSiC software package [33]. Input fugacities were calculated using the Leachman equation of state for normal $H_2$ [34]. Simulations were run for at least $10^7$ MC steps, and care was taken to ensure simulations had reached equilibrium before sampling average properties. Periodic model carbon-based pore systems were generated for cylindrical geometries (SWCNTs in zigzag configuration arranged in a cubic packing that did not allow for interstitial adsorption) and slit pore geometries with explicit carbon atoms. These systems had set pore sizes, as outlined in Table 2, *Supporting Information*, **Figure S11-S12**. The pore size measured in simulation was the separation between carbon atoms on directly opposing pore walls, excluding the van der Waals radii of the carbon atoms. Due to constraints imposed by fixed bond lengths and curvature of the SWCNTs, the pore sizes (0.6 nm, 1.0 mm, 1.2 nm) investigated via modelling differed slightly from the experimental values measured for the SWCNTs (0.7 nm, 1.0 nm, 1.2 nm). Both the carbon frameworks and hydrogen molecules were assumed to be rigid (i.e., bond lengths and angles were kept fixed) and the carbon material was assumed to be defect-free. The system was described using Lennard-Jones potentials only, with standard parameters used for carbon [35] and hydrogen described as a two-site Lennard-Jones model using the parameters of Yang and Zhong [36].

The molecular dynamics simulations were carried out using the DLPOLY 4 [37] code. Initially, each simulation cell was equilibrated in the NVT ensemble, using the Berendsen thermostat, at 77 K. A timestep of 0.5 fs was used over a simulation period of 100 ps. Following this, a 100 ps simulation was undertaken in the NVE ensemble to ensure stability in the NVE ensemble. Each simulation cell was then simulated for 900 ps in the NVE ensemble at 77 K. The mean squared displacement (MSD) of each hydrogen atom, over the first 50 ps, was measured to calculate the diffusion coefficient of hydrogen. The reason for the short time sample was because two different regimes are present. Initially a diffusive regime, over the first 50 ps, and then non-diffusive due to confinement. Additionally, a radial distribution function (RDF) between C and H and between H and H was calculated across the full simulation.

## 3. Results and discussion

### 3.1. Structural characterisation

Three carbon materials were selected, representing three different pore geometries whilst retaining chemically homogeneous adsorption surfaces and comparable pore diameters. The selected samples were a TE7 activated carbon consisting of randomly-ordered graphitic layers (used as a sorption reference material [38]), a titanium carbide-derived carbon (TiC-CDC-800) with slit pore geometry and a sample of single-walled carbon nanotubes (SWCNTs) with cylindrical pore geometry. The SWCNTs were thermally treated to remove the end caps and to allow gas to access the internal porosity. The heating conditions were selected to tune the open porosity and BET surface area of SWCNTs to a level comparable with the other two carbon samples, while also cleaning the surface and removing impurities. All three samples were characterised as follows: Transmission electron microscopy (TEM) was used to demonstrate the differences in pore geometries for these materials, showing the randomly ordered graphitic layers of TE7, the cylindrical pores of SWCNTs and the graphitic layers of TiC-CDC-800, in Fig. 1a–c.

Raman spectra of the three samples in Fig. 2 demonstrate two peaks: the so-called G-peak at ~1590 $cm^{-1}$ and the D-peak at ~1350 $cm^{-1}$. The G-peak is the characteristic feature of the graphitic

**Table 1**
Raman analysis of TiC-CDC-800, TE7 and SWCNT samples.

| Sample | D-peak FWHM ($cm^{-1}$)[a] | G-peak FWHM ($cm^{-1}$)[a] | $I_D/I_G$[b] |
|---|---|---|---|
| TiC-CDC-800 | 265 | 97 | 0.87 |
| TE7 | 205 | 95 | 0.97 |
| SWCNTs | 53 | 72 | 0.05 |

[a] D-peak FWHM and G-peak FWHM is the full width at half maximum of the D-peak and G-peak.
[b] $I_D/I_G$ is the ratio of D- and G-peak intensities.

**Table 2**
Surface area and porosity analysis of TiC-CDC-800, SWCNTs and TE7 carbons.

| | Pore geometry | BET ($m^2\ g^{-1}$) | Total pore volume ($cm^3\ g^{-1}$)[a] | Micropore volume ($cm^3\ g^{-1}$) | Pore size distribution maxima (nm) |
|---|---|---|---|---|---|
| TiC-CDC-800 | Slit | 1107 ± 5 | 0.46 | 0.39 | 0.7 |
| SWCNTs | Cylindrical | 945 ± 5 | 0.89 | 0.38 | 0.7, 1.0, 1.2 |
| TE7 | Disordered | 1234 ± 7 | 1.33 | 0.42 | 0.7, 1.2 |

[a] Total pore volume is measured at $P/P_0 = 0.95$.

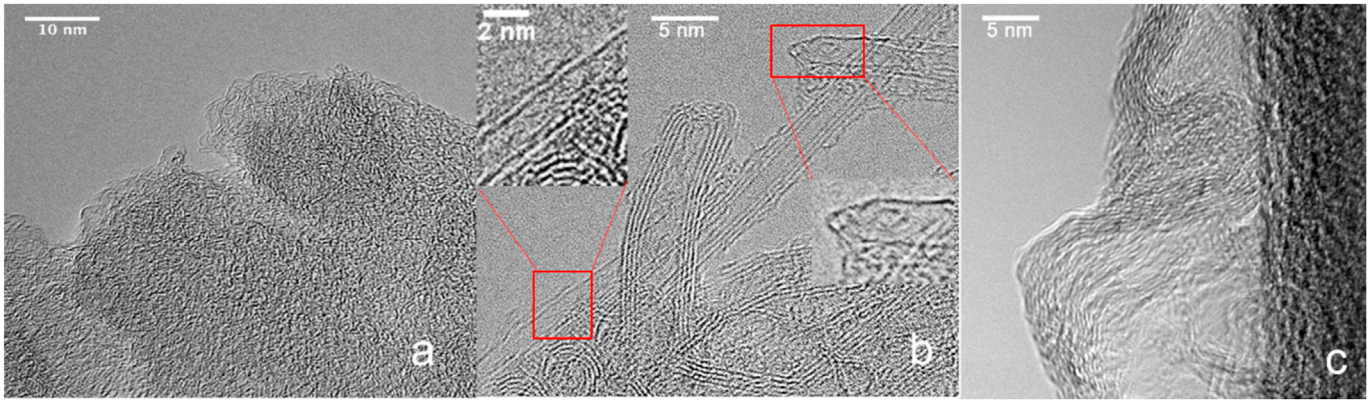


**Fig. 1.** TEM images of (a) TE7 (disordered), (b) SWCNTs (cylindrical pores), with insets highlighting individual SWCNTs, (c) TiC-CDC-800 carbon (slit-shaped pores). (A colour version of this figure can be viewed online.)

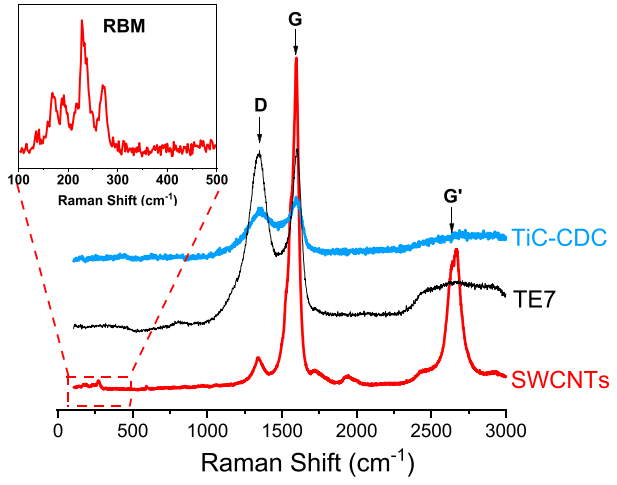


**Fig. 2.** Raman spectra of TiC-CDC-800, TE7, and SWCNTs excited with 514 nm laser radiation. The inset plot shows radial breathing modes (RBMs) of the SWCNTs. (A colour version of this figure can be viewed online.)

layers and corresponds to the tangential vibration of carbon atoms. The D-peak is representative of defective graphitic structures. A comparison of the intensity ratios of these two peaks gives a measure of the quality of the bulk samples. The intensity ratio of D-peak to G-peak ($I_D/I_G$) in Table 1 are indicative of a highly-ordered structure for the SWCNTs and the defective graphitic structure for TE7 and TiC-CDC-800 [39]. The TEM image and Raman results demonstrate that TiC-CDC has a pore structure comprised of defective graphitic sheets.

The Raman spectra of the SWCNTs showed the presence of radial breathing mode (RBM) peaks in the low-frequency range (Fig. 2 inset). In the case of MWCNTs, the signal from radial modes of multiple tubes would be so weak that the RBM peaks would be undetectable by Raman [40,41]; thus, the presence of such modes is evidence of SWCNT or double-walled/few-layer nanotubes. This is consistent with the TEM, in which the presence of SWCNT can be clearly identified (inset Fig. 1b).

The diameter of the nanotubes calculated from the RBM peaks using Equation (1) reported previously [42] varies between 0.6 and 1.2 nm.

$$\omega_{RMB} = \frac{A}{d} + B \tag{1}$$

where $\omega$ is the vibration frequency, $d$ is the nanotube diameter, and $A$ and $B$ are parameters that have different values for individual tubes and tube bundles.

Nitrogen gas sorption measurements were carried out at 77 K to determine the BET surface area and porosity of the three carbons (Fig. 3), as there is a direct correlation between hydrogen adsorption capacity and surface area [43]. The BET surface areas were 1107 $m^2\ g^{-1}$ for TiC-CDC-800, 945 $m^2\ g^{-1}$ for SWCNTs and 1234 $m^2\ g^{-1}$ for TE7. The pore size distributions (PSDs) based on the 2D-NLDFT method are displayed in Fig. 3b, confirming narrowly distributed pore sizes of roughly 0.7 nm diameter for all three materials, and a small proportion of pores with size 1.2 nm for TE7, and 1.0 nm and 1.2 nm for SWCNTs. The pore sizes and pore volumes of these carbons were calculated from $N_2$ gas sorption analysis and are detailed in Table 2.

All samples were tested for purity via thermogravimetric analysis and were confirmed to be > 97 wt% carbon. The TiC-CDC-800 sample exhibited 2.6 wt% remaining after carbon oxidation, corresponding to 0.84 mol% of the precursor (TiC), as shown in Fig. 4. It has been shown previously that the phenolic resin-derived TE7 has very limited surface oxygen groups [44]. The decomposition temperature of TiC-CDC-800 in air was lower than that of SWCNTs and TE7, as reported previously[20].

We used inelastic neutron scattering (INS) with *in situ* gas dosing to experimentally probe the effects of confinement on the behaviour of the very light hydrogen molecules inside the pores of the carbon materials under pressure at cryogenic temperatures

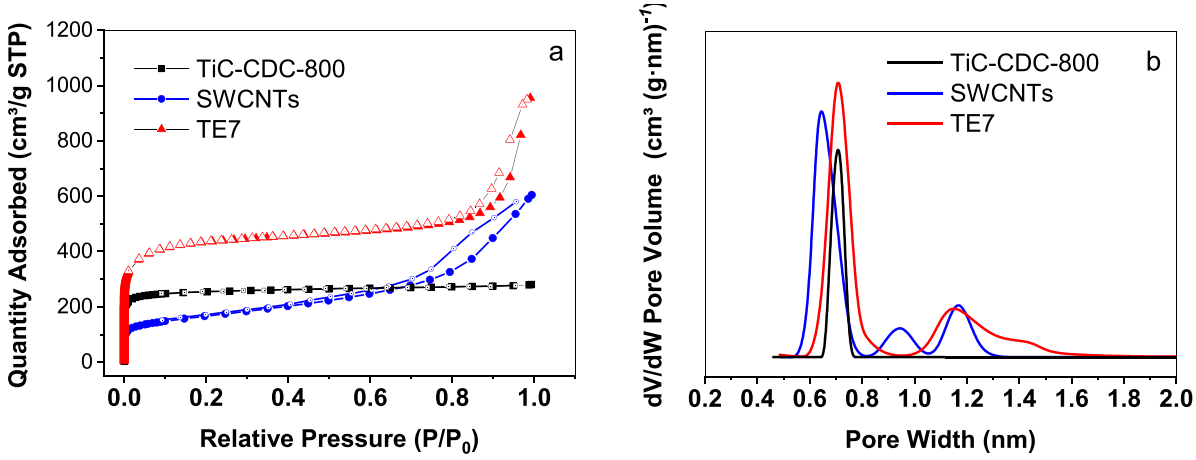


**Fig. 3.** (a) $N_2$ sorption isotherms at 77 K of TiC-CDC-800, TE7, and SWCNTs. The solid symbols represent adsorption, and the open symbols represent desorption. (b) The normalised pore size distribution (PSD) calculated from $N_2$ isotherms using the 2D-NLDFT model. (A colour version of this figure can be viewed online.)

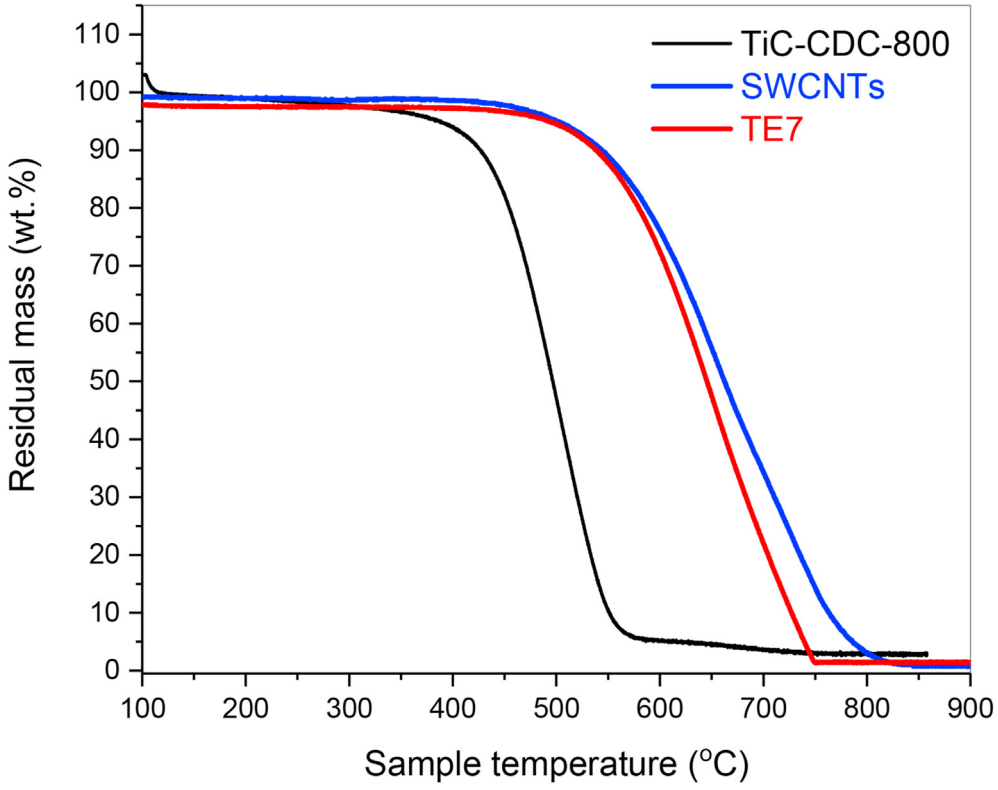


**Fig. 4.** Thermogravimetric analysis (TGA) of the samples measured in flowing air at 5 K $min^{-1}$ ramping rate. (A colour version of this figure can be viewed online.)

[45–47]. Neutrons are highly penetrating, allow the use of high pressure and cryogenic sample environments and, in the case of physisorption of hydrogen, can be used to observe the rotational transitions of adsorbed molecular hydrogen to give information on the state (gaseous, liquid or solid) of the hydrogen inside the pores [23,48,49].

### 3.2. Inelastic neutron scattering and hydrogen adsorption

Normal $H_2$ (i.e., a ratio of 3:1 for *ortho:para* hydrogen spin isomers at room temperature) was used for the *in situ* $H_2$ dosing at 77 K on the three carbons for the INS experiments (Fig. 5 and Fig. 6). Fig. 5a shows the background-subtracted INS spectra of the hydrogen in TiC-CDC-800 up to pressures of 0.3 MPa (i.e., after subtraction of the spectrum contributed by the relevant carbon material under vacuum), demonstrating clear peaks at 0 meV, attributed to the elastic and quasi-elastic scattering of immobile (solid-like) and partially mobile (liquid-like) hydrogen. The spectrum, viewed with a logarithmic energy axis in the inset of Fig. 5a, shows the rotational peaks at 14.7 meV for $H_2$ adsorbed on the TiC-CDC-800 at 77 K and the different pressure loadings. The presence of a rotor peak at 14.7 meV was reported in our previous work on the TE7 reference carbon [22] and corresponds to the $J = 0 \rightarrow 1$ (where $J$ is the rotational quantum number) *para*-to-*ortho*

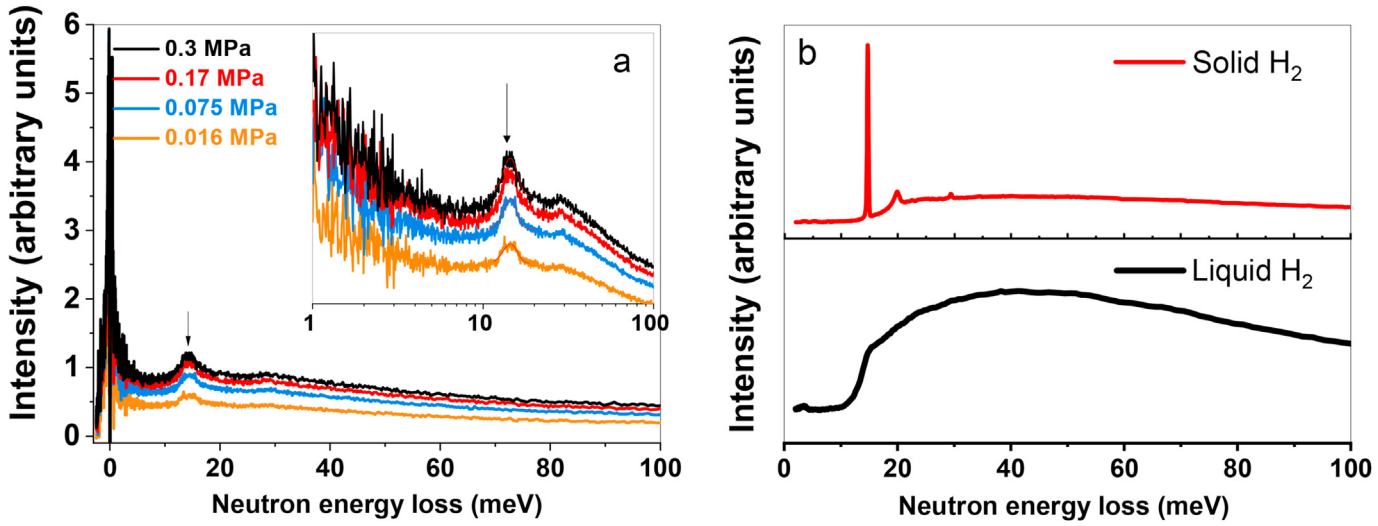


**Fig. 5.** a) INS spectra for $H_2$ adsorbed on TiC-CDC-800 carbon at 77 K in order of increasing $H_2$ pressure from 0.016 MPa to 0.3 MPa. The inserted figure is the magnified low energy region showing the rotor line at 14.7 meV, plotted on a logarithmic scale on the x-axis. (b) INS spectra collected with thermal neutrons on liquid para-$H_2$ (black line) at 14.3 K and solid para-$H_2$ (red line) at 12.2 K, obtained from the ISIS neutron database[54]. The data were collected on TOSCA with the relevant carbon background subtracted. (A colour version of this figure can be viewed online.)

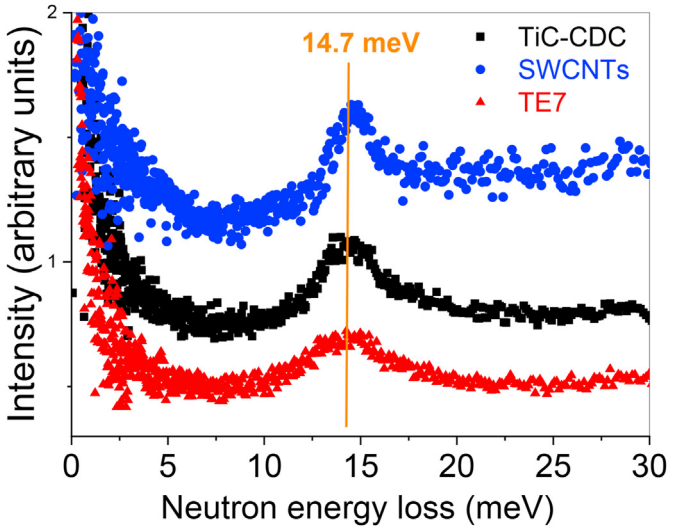


**Fig. 6.** INS spectra of $H_2$ adsorption on TiC-CDC-800 and TE7 at 77 K and 0.016 MPa dosing pressure and at 0.1 MPa hydrogen pressure for SWCNTs, collected on TOSCA. The background for all the INS spectra has been subtracted so the INS spectra show only the scattering from hydrogen. The orange line shows the rotor line at 14.7 meV. (A colour version of this figure can be viewed online.)

rotational transition in solid hydrogen [45,50], observed by both TOSCA and IN4 neutron spectrometers. The presence of 14.7 meV peak suggests that the $H_2$ molecules are in a state where they are fixed in three dimensions and behaving as a free rotor, and thus approximating a solid (hence, 'solid-like'). This significant and sharp rotor peak is characteristic of $H_2$ molecules that are translationally immobilised in all three dimensions, such as with bulk solid hydrogen (Fig. 5b) [22,47]. The "rotor line" contribution at 14.7 meV was also clearly present for $H_2$ on the three carbon materials on all three carbon materials studied on the TOSCA neutron spectrometer (Fig. 6), and was also observed using other neutron spectrometers, for example, the IN4 at the ILL (*Supporting Information*, Figure S1).

From the structure characterisation demonstrated earlier in this work and by other groups, all samples are pure carbon without containing significant amounts of either metal catalysts or surface functional groups [22,51]; therefore, this extreme densification of $H_2$ molecules is solely caused by the confinement in nanopores. The presence of the rotor peak in the INS indicated that the dominant mechanism for sorption was physical adsorption of the H–H molecule, rather than any chemisorption-mediated spillover from defects or edges (which would not present a rotor peak [52]). In addition, over the duration of the INS data collection of 3–6 h, the integrated intensity over the entire INS spectrum was consistent at 77 K at each pressure, indicating that the ratio of *ortho* to *para*-hydrogen was kept at the original 3: 1 ratio [53], further confirming that any defects or terminal carbons were not acting as catalytic sites for *para-ortho* conversion over the timeframe of the experiment. Taken together with the full reversibility of the sorption isotherms (as confirmed via volumetric gas sorption), it was thus safe to assume that the predominant mechanism was physisorption in all three cases, and that any defects in the TE7 and the Ti CDC-800 did not result in any significant chemisorption in the samples.

The elastic scattering and the rotational peaks have been analysed to quantify the proportions of the different $H_2$ phases in the pores. The total neutron scattering intensity in each spectrum was normalised to the number of neutron counts. Hence, the integrated intensity of the INS spectrum is proportional to the total amount of $H_2$ in the sample, including immobile (solid-like), partially mobile (liquid-like) and gas phase. The 'liquid-like' hydrogen is that the hydrogen molecules are in a state where they are have only limited mobility. Gaseous $H_2$ molecules do not scatter elastically but contribute to the total spectral background across the whole energy range. As mentioned, the rotor line is indicative of immobile (solid-like) $H_2$. Integration of this peak, therefore, provides information on the amount of solid-like $H_2$. The integrated intensity of the rotor peak was shown to increase with increasing $H_2$ pressure (up to pressures of 0.3 MPa) for all three samples, indicating an accumulation of immobilised $H_2$ in the pores.

To further determine relative amounts of $H_2$ in different states, we systematically evaluated the integrated intensities over different regions of the INS spectra as a function of pressure (Fig. 7: TiC-CDC-800, Fig. 8: SWCNTs). Detailed information for TE7 can be found in our previous work [22]. The total amount of $H_2$ in and around the TiC-CDC-800 sample was evaluated from the integrated

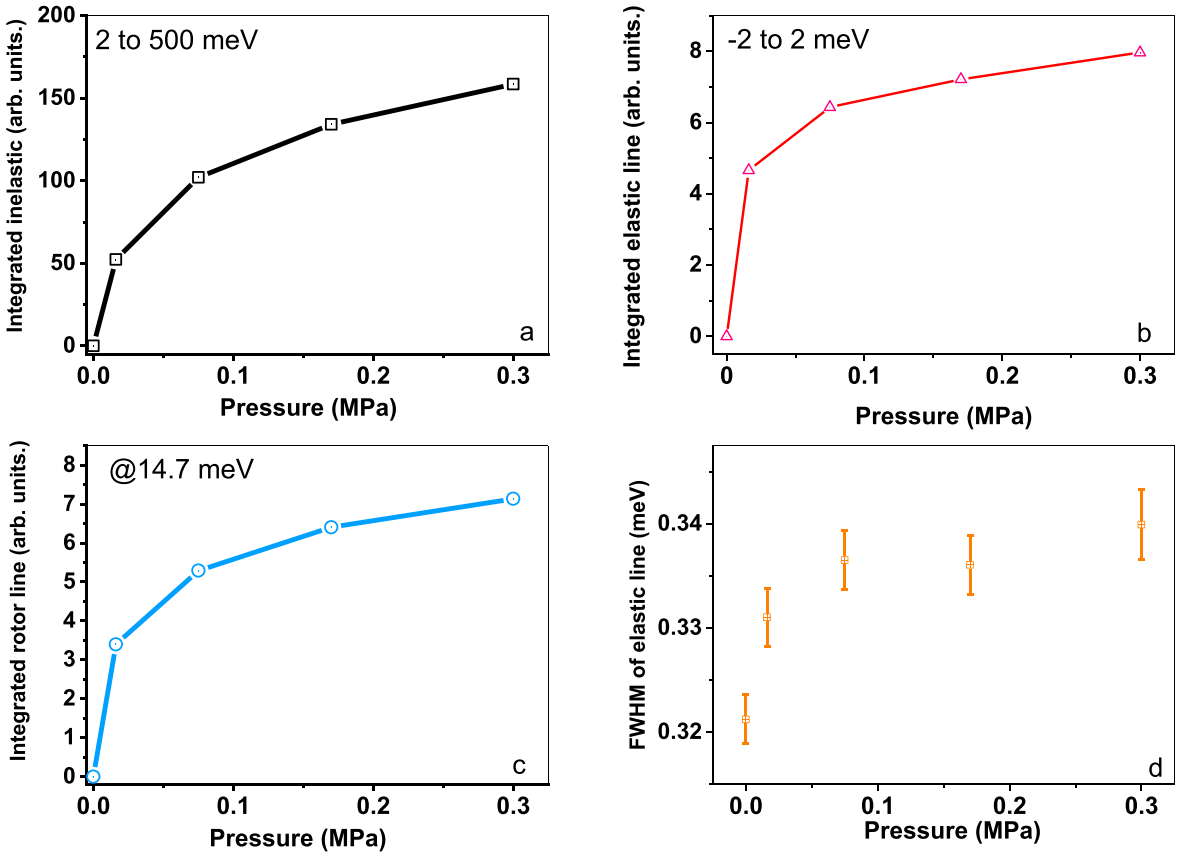


**Fig. 7.** Integrated peak intensities from numerical integration of INS data from TOSCA for TiC-CDC-800 as a function of $H_2$ dosing pressure at 77 K (a) the integrated intensity from 2 meV to 500 meV, (b) integrated intensity under the elastic peak from −2 meV to +2 meV, (c) integrated intensity under the 14.7 meV rotor line from 11 meV to 18 meV, (d) the evolution of the FWHM of the elastic line (0 meV) as a function of $H_2$ dosing pressure at 77 K. (A colour version of this figure can be viewed online.)

intensity over the entire inelastic range from 2 meV to 500 meV and showed a Type I isotherm with increasing $H_2$ pressure (Fig. 7a), demonstrating the total accumulation of solid-like, liquid-like and gaseous hydrogen. The integrated intensity of the rotor line represents the solid-like $H_2$, while the integrated intensity of the elastic peak indicates the amount of the strongly densified $H_2$ (solid-like and liquid-like phases), shown in Fig. 7b and c. Both figures showed a rapid increase in intensity at lower pressure before approaching saturation, typical for a Type 1 isotherm [55]. Saturation is achieved when the micropores are fully filled with the densified $H_2$ at a pressure exceeding 1 MPa as indicated by high-pressure $H_2$ adsorption isotherms (Fig. 9a). The full-width at half-maximum (FWHM) of the elastic peak at the lowest $H_2$ adsorption pressure of 0.016 MPa was 0.330 ± 0.003 meV (Fig. 7d). This value is very close to TOSCA's instrumental resolution of 0.32 meV, and the lack of significant peak broadening indicates the limited mobility of the adsorbed $H_2$. The INS spectra of $H_2$ dosed into slit-shaped pores of TiC-CDC-800 between 0.016 MPa, and 0.3 MPa demonstrated that the quantity of contained, solid-like and liquid-like $H_2$ increased with pressure before its maximum excess adsorption.

The INS spectra of $H_2$ in the SWCNTs at 77 K (Supporting *Information*, Figure S1-S2) presented an elastic line at 0 meV and a rotor peak at 14.7 meV, indicating the presence of both liquid- and solid-like hydrogen in the cylindrical pores at 77 K. It should also be noted that in cases where nanotubes are tightly bundled, strongly binding interstitial sites between adjacent nanotubes can be an important contributing factor [52]. However, the rotor peak in Fig. 6 shows a single peak, rather than the clear bimodal distribution at low pressures that would be indicative of having substantial contributions from two distinct sorption environments (for example, one inside and one at the interstices of neighboring tubes [56]). In addition, the TEM in Fig. 1b indicates the nanotubes are not comprised of well-ordered bundles. Hence, it was assumed that the majority of the densified hydrogen is occupying a single adsorption environment inside the open tubes. The FWHM of the $H_2$ elastic peak of the SWCNTs was 0.44 meV at 0.3 MPa (Fig. 8d). This is broader than was observed for TiC-CDC-800 (0.34 meV at 0.3 MPa, Fig. 7d) as well as the peak width for TE7 (*Supporting Information*, Figure S3), indicating the increased dynamics of $H_2$ in the cylindrical pores. The broader FWHM of the $H_2$ elastic peak results from the increased mobility of $H_2$ molecules in SWCNTs, highlighting that $H_2$ in the SWCNTs is more mobile than $H_2$ confined in slit-shaped pores at 77 K. This result indicates that the packing of $H_2$ in the SWCNTs is less well-ordered than in slit pores, and thus, the density of $H_2$ in the SWCNTs may be lower than in slit pores. After the initial rise of the FWHM of the elastic peak the SWCNTs over the pressure range 0.01–0.3 MPa in Fig. 8b, the FWHM decreases at 2 MPa, suggesting an increase in the proportion of liquid-like $H_2$ at higher pressure.

It was also noted that the integrated intensity across the inelastic range (Fig. 8a) showed a rapid increase at high pressure, resulting from the accumulation of gaseous hydrogen [34]. This notable accumulation of gaseous $H_2$ for the cylindrical pores indicated that there was a substantial amount of hydrogen in the sample that was outside the nanotubes, and therefore not confined.

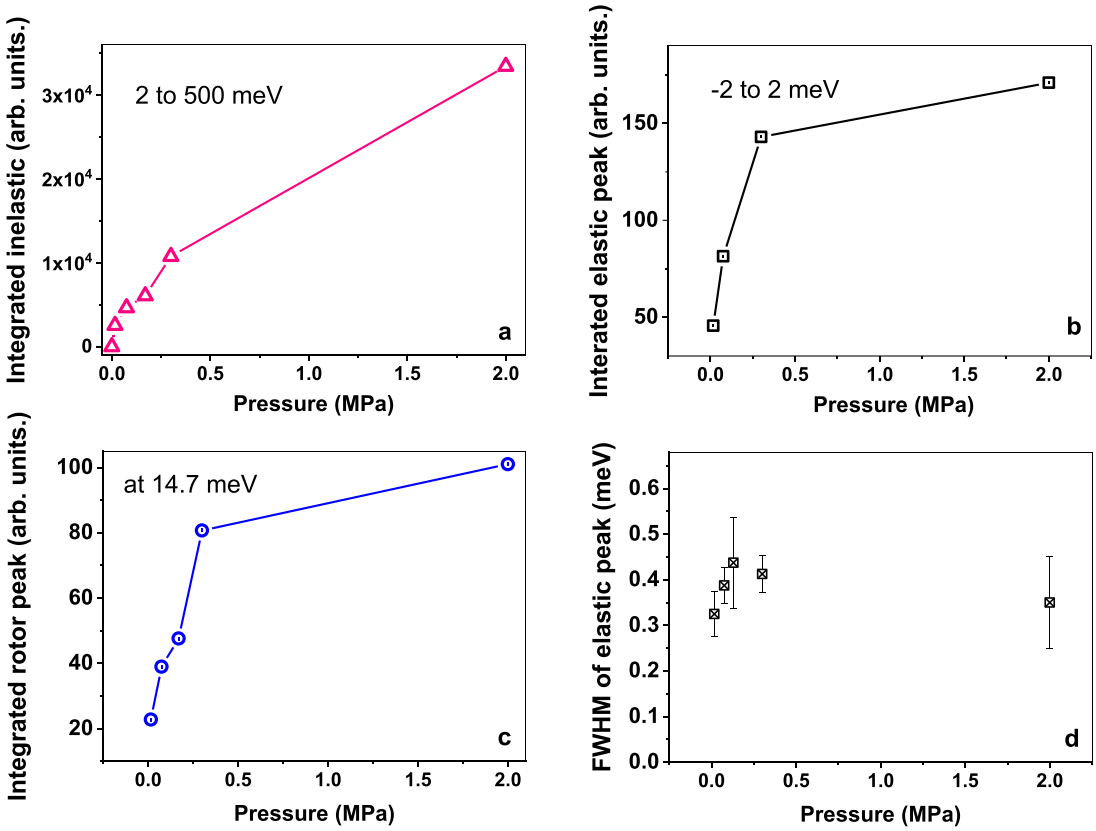


**Fig. 8.** Integrated peak intensities from numerical integration of INS data for SWCNTs as a function of $H_2$ dosing pressure at 77 K (a) the integrated intensity from 2 meV to 500 meV, (b) integrated intensity under the elastic peak from −2 meV to +2 meV, (c) integrated intensity under the 14.7 meV rotor line from 11 meV to 18 meV; (d) the evolution of the FWHM of the elastic line (0 meV) as a function of $H_2$ dosing pressure at 77 K. The data were collected on TOSCA. (A colour version of this figure can be viewed online.)

The densities of the bulk hydrogen not confined within the nanotubes (equal to the bulk hydrogen density) were 0.32 kg $m^{-3}$ and 0.95 kg $m^{-3}$ at 0.1 MPa and 0.3 MPa, respectively [57]. Consequently, the average density of $H_2$ in the SWCNTs is the average of this liquid-like, solid-like and gaseous hydrogen, which results in lower overall densities when compared to the average density in the slit-shaped pores. The ratio of the integrated intensity under the rotor peak to the entire inelastic area indicates the ratio of solid-like $H_2$ to total $H_2$ in and around the sample (Supporting *Information*, Figure S4). The ratio of solid-like $H_2$ to the total $H_2$ for TiC-CDC-800 is five times higher than for the SWCNTs, suggesting higher overall $H_2$ density in TiC-CDC-800.

Hydrogen storage capacities of the samples were evaluated through high-pressure $H_2$ adsorption isotherms of TiC-CDC-800, SWCNTs, and TE7 measured at 77 K (Fig. 9a). Subsequently, the experimental Gibbs excess isotherms for $H_2$ adsorbed at 77 K were modelled using a semi-empirical methodology [51], and then converted to absolute $H_2$ uptake (Fig. 9b–d). During the $H_2$ isotherm fitting, the average density of the adsorbed $H_2$ in the pores was obtained. The fitting equations are detailed in the supporting information and illustrated in *Supporting Information*, Figure S5-S7.

The estimated average density at maximum adsorption refers, in particular, to the total adsorbate mass divided by pore volume, which covers all of the $H_2$ in the pores including highly densified $H_2$ on the pore wall as well as less strongly adsorbed $H_2$. The estimate of the adsorbed $H_2$ density on TE7 from fitting the experimental isotherm to the Toth equation was 101 kg $m^{-3}$, which is significantly higher than the maximum density of liquid $H_2$ of 70 kg $m^{-3}$ (at 14 K and 7.36 kPa [34]) and is above the density of bulk solid $H_2$ of 87 kg $m^{-3}$ (at 12 K) [58,59]. The high density of the adsorbed $H_2$ in the pores was expected from the dense packing of hydrogen molecules due to pore confinement. The average $H_2$ densities on TiC-CDC-800 and SWCNTs were calculated as 70 kg $m^{-3}$ and 50 kg $m^{-3}$, respectively, corresponding to average densities at maximum adsorption similar to liquid hydrogen; these values are consistent with our investigation from INS and the findings of Gogotsi et al.[2], confirming the presence of densified $H_2$ phase in pores alongside less densely packed $H_2$.

These densities of highly confined hydrogen at 77 K indicate an effectively liquid fraction of hydrogen at temperatures (i.e., 77 K) far above the critical temperature (33 K) and under conditions where liquefaction should not be possible in bulk. Carbon nanomaterials are known to have low isosteric enthalpies of adsorption (typically 5–10 kJ $mol^{-1}$) [60,61] indicating that the binding strength of hydrogen on carbon alone is not likely a major contributing factor for the extremely high levels of densification. In the absence of tightly packed nanotube bundles which could afford very specific adsorption sites at the intersections of the tubes [62] or surface functional groups, the densification of $H_2$ inside the porous carbons at 77 K is expected to be purely due to confinement in the optimally sized pores.

### 3.3. Monte Carlo and molecular dynamics simulations

To clarify the differences in density of adsorbate, the adsorption of $H_2$ molecules inside micropores with pore sizes and geometries consistent with experiment was explored *via* Monte Carlo (MC) and molecular dynamics simulations (MD). The MC simulated the

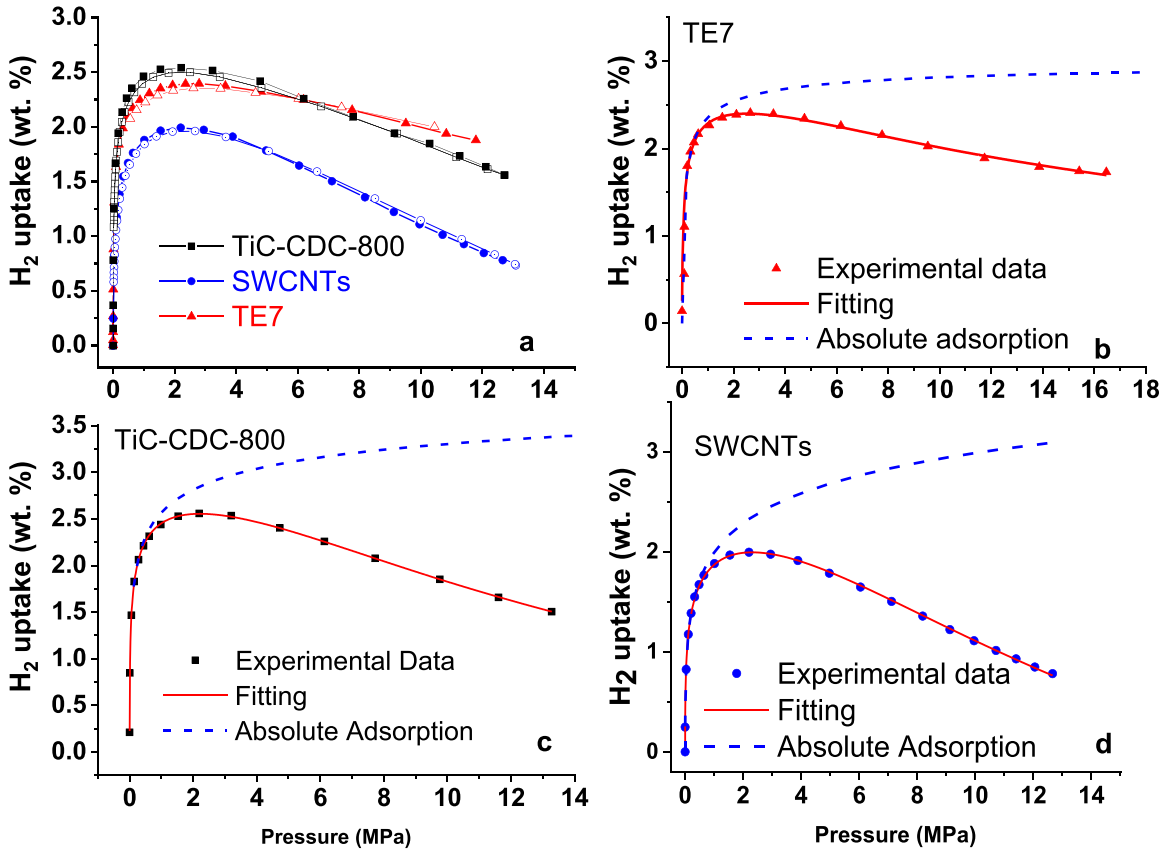


**Fig. 9.** (a) Experimental excess $H_2$ sorption isotherm at 77 K for TiC-CDC-800, SWCNTs, and TE7 carbons. Experimental excess $H_2$ uptake as a function of pressure and modelling at 77 K for (b) TE7, (c) TiC-CDC-800, and (d) SWCNTs. The red triangles, the black squares, and the blue circles represent the experimentally measured excess adsorption isotherms of TE7, TiC-CDC-800, and SWCNTs, respectively; the solid red lines are the fitted isotherms, and the blue dashed lines represent the calculated absolute uptake. (A colour version of this figure can be viewed online.)

density of $H_2$ and degree of confinement at saturation was found to be comparable in both types of pore geometry for 0.7 nm pores (~82 kg $m^3$ for both cylindrical and slit pores). The predicted $H_2$ density (denser than liquid $H_2$) is consistent with the INS experiments, which showed solid-like $H_2$ adsorbed within the pores of TiC-CDC-800 (slit pores) and SWCNTs (cylindrical pores).

Both the Monte-Carlo (MC) simulations and molecular dynamic (MD) simulation revealed hydrogen molecules form two highly ordered and well-defined layers within slit-shaped pores at pore size < 1 nm (Fig. 10). This is consistent with the recent work by Olsen et al. [63] who observed a $H_2$ phase transition in the slit-shaped pore with a width of 0.5–0.65 nm at 75 K. They demonstrated the formation of a commensurate solid of orientationally ordered *ortho*-$H_2$ with a bilayer structure through INS experiment and hydrogen adsorption [63].

Both MC and MD simulations of hydrogen molecules in the 0.66 nm diameter nanotubes showed a similarly well-defined packing arrangement along the length of the nanotube (Fig. 10). The packing of $H_2$ molecules within cylindrical pores was found to be strongly influenced by small changes in the pore diameter. Increasing the pore diameter to 0.99 nm and 1.16 nm (i.e., corresponding to the additional peaks present in the experimental PSD, Fig. 3b) resulted in the formation of a less well-defined secondary $H_2$ layer in the pores, as well as in the increase in disorder of the monolayer near the pore wall (Fig. 10).

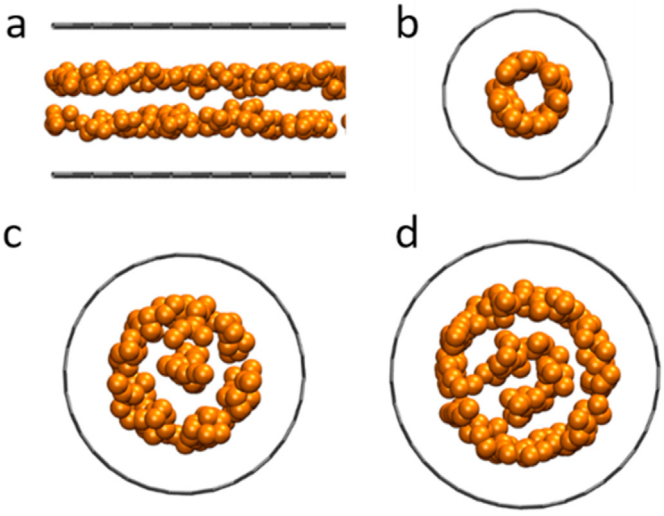


**Fig. 10.** Favourable packing and orientations obtained from MC simulations of $H_2$ confined in (a) slit-shaped pores at a pore size of 0.66 nm and in cylindrical pores at pore sizes of 0.60 nm (b), 0.99 nm (c), and 1.16 nm (d). Hydrogen molecules are represented by single golden spheres, and carbon atoms are shown as grey sticks. (A colour version of this figure can be viewed online.)

In the MC calculations, the larger pores were found to be of particular relevance above a $H_2$ partial pressure of ~1 MPa (Supporting *Information*, Figure S8). At this point, the smallest pore was nearly fully saturated, while the larger diameter pores were only ~75% filled (i.e., any $H_2$ being adsorbed at higher dosing pressures is likely to enter into the larger pores and therefore be less strongly confined). This is consistent with the plateau in rotor peak intensity and continued broadening of the elastic peak observed in INS experiments (Figs. 7b and 8b).

However, we noted that the hydrogen density in the cylindrical pores with a pore size of 0.7 nm obtained from the MC simulation (82 kg $m^3$) was higher than that calculated from the experimental data fitting (50 kg $m^3$). This can be explained by differences in the sample between simulations and the experiment. In the simulation, a simplified finite geometry of the cylindrical pore shape and square-packed SWCNT arrays with the circumference of each pore in contact with its neighbour were employed (Supporting *Information*, Figure S11). This cylindrical unit cell was rigid and assumed a close packed array which did not consider the random orientation of the nanotubes. Experimentally, the SWCNTs were flexible and randomly oriented, resulting in increased void space outside the carbon nanotubes. Therefore, the experimental density was calculated to be significantly lower than the molecular simulation result.

We also used MD simulations to investigate hydrogen dynamics inside the pores. The mean square displacement (MSD) was calculated, which characterises the movement and diffusion of hydrogen molecules (Supporting *Information*, Figure S14). The $H_2$ adsorption on slit-shaped and cylindrical pores fall into two different groups with $H_2$ in the SWCNTs showing slower diffusion, as indicated by the gradient of the slope in the diffusive regime (the first ~20 ps of the simulation), and $H_2$ in the slit-shaped pores showing faster diffusion. The plateaus indicate a confinement effect. Based on the MSD, the self-diffusion coefficients were calculated using the Einstein relation as shown in Supporting *Information*, Table S2, giving a higher diffusion coefficient of $H_2$ by a factor of ~2 in the slit-shaped pores compared to the cylindrical pores. This result is consistent with the transport properties of $H_2$ confined in carbide-derived carbons with different pore shapes and size, reported by Harmas et al. [10] Within the cylindrical pores, hydrogen has significant directional constraints due to the geometry of the space, whereas in the slit pores, hydrogen is able to explore more of the space available without surface/molecule interactions restricting the dimensionality of translational motion. This restriction in movement results in the reduced diffusivity within the CNTs (Supporting *Information*, Figure S9-S10). In a more open system, this difference in mobility may be considered significant in determining more macroscopic experimental observations. However, the magnitude and early on-set of the observed confining effects in both systems appear to be the dominating factors from our simulations.

The simulations suggest small differences in order and mobility of hydrogen confined in the three perfect systems. Overall, both the MC and MD simulations confirmed the formation of highly ordered $H_2$ structure in both pore shapes within the experimental pore size range. MD suggests that the mobility of $H_2$ molecules in the SWCNTs at a pore size of 0.58 nm is lower than in the slit pore systems due to geometric constraints, while the significant confining effect on mobility is very clear in both systems and will likely be the dominating factor in our more macroscopic observations. The differences in ordering of hydrogen molecules in the two pore shapes are subtle and difficult to properly contrast, as shown in the calculated radial distribution function (RDF) plot in Supporting *Information*, Figure S13. Perfect, rigid, and defect-free systems were used in these simulations, resulting in the discrepancies seen in $H_2$ density between the simulations and experiment.

## 4. Conclusion

To summarise, our studies confirm that confinement in pores can have a strong influence on gas/liquid and liquid/solid phase transitions, even in the case of a weakly-interacting molecule such as hydrogen. Through the combination of in-situ INS, high-pressure gas sorption experiments and simulations, we have systematically investigated the effects of pore geometry and pore size on the density and mobility of $H_2$ in the microporous carbon materials, contrasting and comparing the slit-like pores found in TiC-CDC-800 with the cylindrical pores found in SWCNTs and the disordered structure of TE7 carbon. For all pore geometries, spectral features consistent with the accumulation of densified $H_2$ were observed at 77 K and pressures as low as 0.016 MPa. The results were complemented by the molecular dynamics simulation and Monte Carlo simulations of $H_2$ inside different pore geometries, where $H_2$ behaviour was found to be strongly influenced by small pore size (<1 nm).

The MD and MC simulations demonstrated that SWCNTs with a pore size around 0.58 nm led to the highest degree of hydrogen ordering among the geometries studied here. The simulations also suggested that subtle differences in order and mobility exist between the two pore geometries. Therefore, a narrow pore size distribution (<1 nm) remains the most crucial factor for maximising hydrogen density and capacity of porous materials. It is suggested particularly during industrial manufacture, tuning pore size of porous material to less than 1 nm should be the main consideration for gas adsorption, rather than costly control of homogenous pore shape.

In conclusion, this study sheds new light on confined hydrogen behaviour at supercritical conditions. The results demonstrate that the pore size remains the key factor when optimising hydrogen densities in pores for high capacity $H_2$ storage applications. However, pore geometry may represent another consideration for high density gas phase transition for other applications, e.g. controlling hydrogen crystallisation.

## Supporting Information

Supporting Information includes modelling of high-pressure $H_2$ uptake isotherms, snapshots of molecular simulation and INS spectra.

## Data availability

INS data DOI: 10.5286/ISIS.E.RB1720219 and 10.5286/ISIS.E.RB1610401.

## CRediT authorship contribution statement

**Mi Tian:** Methodology, Investigation, Writing - original draft, Funding acquisition. **Matthew J. Lennox:** Formal analysis. **Alexander J. O'Malley:** Formal analysis. **Alexander J. Porter:** Formal analysis. **Benjamin Krüner:** Investigation. **Svemir Rudić:** Investigation, Writing - review & editing. **Timothy J. Mays:** Supervision, Funding acquisition. **Tina Düren:** Supervision. **Volker Presser:** Investigation, Writing - review & editing. **Lui R. Terry:** Investigation, Writing - review & editing. **Stephane Rols:** Investigation. **Yanan Fang:** Investigation. **Zhili Dong:** Investigation. **Sebastien Rochat:** Investigation, Writing - review & editing. **Valeska P. Ting:** Conceptualization, Writing - review & editing, Supervision, Funding acquisition.

## Declaration of competing interest

The authors declare that they have no known competing financial interests or personal relationships that could have appeared to influence the work reported in this paper.

## Acknowledgement

The authors acknowledge funding from the EPSRC H2FC SUPERGEN Hub (EP/E040071/1, EP/L016354/1, EP/L08365/1, EP/K021109/1, EP/J016454/1) for VPT and MT, an EPSRC Research Fellowship for VPT (EP/R01650X/1), funding from the STFC for beamtime on TOSCA (RB1410602 and RB1610401) and from the ILL (7-05-468) for beamtime on IN4. We also thank Dr Chris Goodway and Dr Mark Kibble (STFC) for user support at ISIS, and Prof. Steve Tennison at CarbonTex for the TE7 carbon beads. VP and BK thank Eduard Arzt (INM) for his continuing support. AJOM acknowledges Roger and Sue Whorrod for the funding of the Whorrod Fellowship. This research made use of the Balena High Performance Computing (HPC) Service at the University of Bath.

## Appendix A. Supplementary data

Supplementary data to this article can be found online at https://doi.org/10.1016/j.carbon.2020.11.063.

## References

[1] G. Sethia, A. Sayari, Activated carbon with optimum pore size distribution for hydrogen storage, Carbon 99 (2016) 289–294.
[2] Y. Gogotsi, C. Portet, S. Osswald, J.M. Simmons, T. Yildirim, G. Laudisio, J.E. Fischer, Importance of pore size in high-pressure hydrogen storage by porous carbons, Int. J. Hydrogen Energy 34 (15) (2009) 6314–6319.
[3] C. Zhou, J.A. Szpunar, X. Cui, Synthesis of Ni/graphene nanocomposite for hydrogen storage, ACS Appl. Mater. Interfaces 8 (24) (2016) 15232–15241.
[4] V. Tozzini, V. Pellegrini, Prospects for hydrogen storage in graphene, Phys. Chem. Chem. Phys. 15 (1) (2013) 80–89.
[5] A. Naeem, V.P. Ting, U. Hintermair, M. Tian, R. Telford, S. Halim, H. Nowell, M. Holynska, S.J. Teat, I.J. Scowen, S. Nayak, Mixed-linker approach in designing porous zirconium-based metal-organic frameworks with high hydrogen storage capacity, Chem. Commun. 52 (50) (2016) 7826–7829.
[6] S. Rochat, K. Polak-Krasna, M. Tian, L.T. Holyfield, T.J. Mays, C.R. Bowen, A.D. Burrows, Hydrogen storage in polymer-based processable microporous composites, J. Mater. Chem. 5 (35) (2017) 18752–18761.
[7] D. Ramimoghadam, E.M. Gray, C.J. Webb, Review of polymers of intrinsic microporosity for hydrogen storage applications, Int. J. Hydrogen Energy 41 (38) (2016) 16944–16965.
[8] M. Tian, S. Rochat, K. Polak-Kraśna, L.T. Holyfield, A.D. Burrows, C.R. Bowen, T.J. Mays, Nanoporous polymer-based composites for enhanced hydrogen storage, Adsorption 25 (4) (2019) 889–901.
[9] E. Van Cleve, M.A. Worsley, S.O. Kucheyev, Liquid–solid phase transition of hydrogen and deuterium in silica aerogel, J. Appl. Phys. 116 (16) (2014) 163517.
[10] R. Härmas, R. Palm, M. Russina, H. Kurig, V. Grzimek, E. Härk, M. Koppel, I. Tallo, M. Paalo, O. Oll, J. Embs, E. Lust, Transport properties of H2 confined in carbide-derived carbons with different pore shapes and sizes, Carbon 155 (2019) 122–128.
[11] M. Erko, G.H. Findenegg, N. Cade, A.G. Michette, O. Paris, Confinement-induced structural changes of water studied by Raman scattering, Phys. Rev. B 84 (10) (2011) 104205.
[12] J. Liu, L. Feng, X. Wang, M. Zhao, Exploring the effect of confinement on water clusters in carbon nanotubes, J. Mol. Model. 23 (4) (2017) 133.
[13] A. Striolo, K.E. Gubbins, A.A. Chialvo, P.T. Cummings, Simulated water adsorption isotherms in carbon nanopores, Mol. Phys. 102 (3) (2004) 243–251.
[14] W.H. Noon, K.D. Ausman, R.E. Smalley, J. Ma, Helical ice-sheets inside carbon nanotubes in the physiological condition, Chem. Phys. Lett. 355 (5) (2002) 445–448.
[15] D. Takaiwa, I. Hatano, K. Koga, H. Tanaka, Phase diagram of water in carbon nanotubes, Proc. Natl. Acad. Sci. Unit. States Am. 105 (1) (2008) 39.
[16] S. Choi, M.A. Alkhabbaz, Y. Wang, R.M. Othman, M. Choi, Unique thermal contraction of zeolite-templated carbons enabling micropore size tailoring and its effects on methane storage, Carbon 141 (2019) 143–153.
[17] Y. Kondo, M. Schindler, F. Pobell, Hydrogen in an oscillating porous Vycor glass, J. Low Temp. Phys. 101 (1) (1995) 195–204.
[18] S.O. Kucheyev, E.V. Cleve, M.A. Worsley, Freezing and melting of hydrogen confined in nanoporous silica, J. Phys. Condens. Matter 26 (22) (2014) 225004.
[19] I. Cabria, M.J. López, J.A. Alonso, The optimum average nanopore size for hydrogen storage in carbon nanoporous materials, Carbon 45 (13) (2007) 2649–2658.
[20] S. Choudhury, B. Krüner, P. Massuti-Ballester, A. Tolosa, C. Prehal, I. Grobelsek, O. Paris, L. Borchardt, V. Presser, Microporous novolac-derived carbon beads/sulfur hybrid cathode for lithium-sulfur batteries, J. Power Sources 357 (2017) 198–208.
[21] G. Yushin, R. Dash, J. Jagiello, J.E. Fischer, Y. Gogotsi, Carbide-derived carbons: effect of pore size on hydrogen uptake and heat of adsorption, Adv. Funct. Mater. 16 (17) (2006) 2288–2293.
[22] V.P. Ting, A.J. Ramirez-Cuesta, N. Bimbo, J.E. Sharpe, A. Noguera-Diaz, V. Presser, S. Rudic, T.J. Mays, Direct evidence for solid-like hydrogen in a nanoporous carbon hydrogen storage material at supercritical temperatures, ACS Nano 9 (8) (2015) 8249–8254.
[23] J. Rogacka, L. Firlej, B. Kuchta, Modeling of low temperature adsorption of hydrogen in carbon nanopores, J. Mol. Model. 23 (1) (2017) 20.
[24] M.A. Balderas Altamirano, S. Cordero, R. López-Esparza, E. Pérez, A. Gama Goicochea, Importance of pore length and geometry in the adsorption/desorption process: a molecular simulation study, Mol. Phys. 113 (23) (2015) 3849–3853.
[25] E.-J. Lee, R.-W. Chang, J.-H. Han, T.-D. Chung, Effect of pore geometry on gas adsorption: Grand canonical Monte Carlo simulation studies, Bull. Kor. Chem. Soc. 33 (3) (2012) 901–905.
[26] I. Cabria, M.J. López, J.A. Alonso, Simulation of the hydrogen storage in nanoporous carbons with different pore shapes, Int. J. Hydrogen Energy 36 (17) (2011) 10748–10759.
[27] Y. Long, M. Śliwińska-Bartkowiak, H. Drozdowski, M. Kempiński, K.A. Phillips, J.C. Palmer, K.E. Gubbins, High pressure effect in nanoporous carbon materials: effects of pore geometry, Colloid. Surface. Physicochem. Eng. Aspect. 437 (2013) 33–41.
[28] J. Jagiello, M. Thommes, Comparison of DFT characterization methods based on N2, Ar, CO2, and H2 adsorption applied to carbons with various pore size distributions, Carbon 42 (7) (2004) 1227–1232.
[29] B. Raghavan, T. Gupta, H2/CH4 gas separation by variation in pore geometry of nanoporous graphene, J. Phys. Chem. C 121 (3) (2017) 1904–1909.
[30] J. Rouquerol, P. Llewellyn, F. Rouquerol, Is the bet equation applicable to microporous adsorbents? in: P.L. Llewellyn, F. Rodriquez-Reinoso, J. Rouqerol, N. Seaton (Eds.), Studies in Surface Science and Catalysis Elsevier, 2007, pp. 49–56.
[31] S.F. Parker, F. Fernandez-Alonso, A.J. Ramirez-Cuesta, J. Tomkinson, S. Rudic, R.S. Pinna, G. Gorini, J. Fernández Castañon, Recent and future developments on TOSCA at ISIS, J. Phys. Conf. 554 (2014), 012003.
[32] R.S. Pinna, S. Rudić, S.F. Parker, J. Armstrong, M. Zanetti, G. Škoro, S.P. Waller, D. Zacek, C.A. Smith, M.J. Capstick, D.J. McPhail, D.E. Pooley, G.D. Howells, G. Gorini, F. Fernandez-Alonso, The neutron guide upgrade of the TOSCA spectrometer, Nucl. Instrum. Methods Phys. Res. Sect. A Accel. Spectrom. Detect. Assoc. Equip. 896 (2018) 68–74.
[33] A. Gupta, S. Chempath, M.J. Sanborn, L.A. Clark, R.Q. Snurr, Object-oriented programming paradigms for molecular modeling, Mol. Simulat. 29 (1) (2003) 29–46.
[34] J.W.J. Leachman, T. R, S.G. Penoncello, Fundamental equations of state for parahydrogen, normal hydrogen, and orthohydrogen, J. Phys. Chem. Ref. Data 38 (3) (2009) 721–748.
[35] M.J. Bojan, A.V. Vernov, W.A. Steele, Simulation studies of adsorption in rough-walled cylindrical pores, Langmuir 8 (3) (1992) 901–908.
[36] Q. Yang, C. Zhong, Molecular simulation of adsorption and diffusion of hydrogen in Metal–Organic frameworks, J. Phys. Chem. B 109 (24) (2005) 11862–11864.
[37] I.T. Todorov, W. Smith, K. Trachenko, M.T. Dove, DL_POLY_3: new dimensions in molecular dynamics simulations via massive parallelism, J. Mater. Chem. 16 (20) (2006) 1911–1918.
[38] A. Hruzewicz-Kołodziejczyk, V.P. Ting, N. Bimbo, T.J. Mays, Improving comparability of hydrogen storage capacities of nanoporous materials, Int. J. Hydrogen Energy 37 (3) (2012) 2728–2736.
[39] L. Bokobza, J.-L. Bruneel, M. Couzi, Raman spectroscopy as a tool for the analysis of carbon-based materials (highly oriented pyrolitic graphite, multilayer graphene and multiwall carbon nanotubes) and of some of their elastomeric composites, Vib. Spectrosc. 74 (2014) 57–63.
[40] X. Zhao, Y. Ando, L.-C. Qin, H. Kataura, Y. Maniwa, R. Saito, Radial breathing modes of multiwalled carbon nanotubes, Chem. Phys. Lett. 361 (1) (2002) 169–174.
[41] S. Suzuki, H. Hibino, Characterization of doped single-wall carbon nanotubes by Raman spectroscopy, Carbon 49 (7) (2011) 2264–2272.
[42] M.S. Dresselhaus, G. Dresselhaus, A. Jorio, A.G. Souza Filho, M.A. Pimenta, R. Saito, Single nanotube Raman spectroscopy, Acc. Chem. Res. 35 (12) (2002) 1070–1078.
[43] E. Poirier, R. Chahine, T.K. Bose, Hydrogen adsorption in carbon nanostructures, Int. J. Hydrogen Energy 26 (8) (2001) 831–835.
[44] A. Pigamo, M. Besson, B. Blanc, P. Gallezot, A. Blackburn, O. Kozynchenko, S. Tennison, E. Crezee, F. Kapteijn, Effect of oxygen functional groups on synthetic carbons on liquid phase oxidation of cyclohexanone, Carbon 40 (8) (2002) 1267–1278.
[45] P.C.H. Mitchell, S.F. Parker, A.J. Ramirez-Cuesta, J. Tomkinson, Vibrational spectroscopy with neutrons: with applications in chemistry, biology,

materials science and catalysis, Series on neutron techniques and applications 3 (2005) 642.
[46] A.J. Ramirez-Cuesta, M.O. Jones, W.I.F. David, Neutron scattering and hydrogen storage, Mater. Today 12 (11) (2009) 54–61.
[47] J. Bahadur, C.I. Contescu, A.J. Ramirez-Cuesta, E. Mamontov, N.C. Gallego, Y. Cheng, L.L. Daemen, Y.B. Melnichenko, Properties of immobile hydrogen confined in microporous carbon, Carbon 117 (2017) 383–392.
[48] H. Lee, Y.N. Choi, S.B. Choi, J. Kim, D. Kim, D.H. Jung, Y.S. Park, K.B. Yoon, Liquid-like hydrogen stored in nanoporous materials at 50 K observed by in situ neutron diffraction experiments, J. Phys. Chem. C 117 (6) (2013) 3177–3184.
[49] D. Colognesi, M. Celli, A.J. Ramirez-Cuesta, M. Zoppi, Lattice vibrations of para-hydrogen impurities in a solid deuterium matrix: an inelastic neutron scattering study, Phys. Rev. B 76 (17) (2007) 174304.
[50] M. Celli, D. Colognesi, M. Zoppi, Experimental determination of the translational kinetic energy of liquid and solid hydrogen, The European Physical Journal B - Condensed Matter and Complex Systems 14 (2) (2000) 239–244.
[51] J.E. Sharpe, N. Bimbo, V.P. Ting, A.D. Burrows, D. Jiang, T.J. Mays, Supercritical hydrogen adsorption in nanostructured solids with hydrogen density variation in pores, Adsorption 19 (2) (2013) 643–652.
[52] C. Liu, H.-M. Cheng, Carbon nanotubes for clean energy applications, J. Phys. Appl. Phys. 38 (14) (2005) R231–R252.
[53] G. Romanelli, S. Rudić, M. Zanetti, C. Andreani, F. Fernandez-Alonso, G. Gorini, M. Krzystyniak, G. Škoro, Measurement of the para-hydrogen concentration in the ISIS moderators using neutron transmission and thermal conductivity, Nucl. Instrum. Methods Phys. Res. Sect. A Accel. Spectrom. Detect. Assoc. Equip. 888 (2018) 88–95.
[54] S.T.F.C. ISIS, Neutron and Moun Source, UK, INS database, 2019. Accessed, https://www.isis.stfc.ac.uk/Pages/INS-database.aspx. (Accessed 24 January 2019).
[55] M. Thommes, K. Kaneko, V. Neimark Alexander, P. Olivier James, F. Rodriguez-Reinoso, J. Rouquerol, S.W. Sing Kenneth, Physisorption of gases, with special reference to the evaluation of surface area and pore size distribution (IUPAC Technical Report), Pure Appl. Chem. (2015) 1051.
[56] P.A. Georgiev, D.K. Ross, A.D. Monte, U. Montaretto-Marullo, R.A.H. Edwards, A.J. Ramirez-Cuesta, D. Colognesi, Hydrogen site occupancies in single-walled carbon nanotubes studied by inelastic neutron scattering, J. Phys. Condens. Matter 16 (8) (2004) L73–L78.
[57] William E. Acree, Jr., James S. Chickos, Thermophysical Properties of Fluid Systems, in NIST Chemistry WebBook, NIST Standard Reference Database Number 69, Eds. P.J. Linstrom and W.G. Mallard, National Institute of Standards and Technology, Gaithersburg MD, 20899, https://doi.org/10.18434/T4D303, (retrieved November 30, 2020).
[58] I.F. Silvera, The solid molecular hydrogens in the condensed phase: fundamentals and static properties, Rev. Mod. Phys. 52 (2) (1980) 393–452.
[59] S. Institute for Basic, H.M. Roder, Survey of the Properties of the Hydrogen Isotopes below Their Critical Temperatures, U.S. Dept. of Commerce, National Bureau of Standards, Washington, 1973.
[60] A. Matsumoto, K. Yamamoto, T. Miyata, Microcalorimetric characterization of hydrogen adsorption on nanoporous carbon materials, in: P.L. Llewellyn, F. Rodriquez-Reinoso, J. Rouqerol, N. Seaton (Eds.), Studies in Surface Science and Catalysis, Elsevier, 2007, pp. 121–128.
[61] N. Bimbo, J.E. Sharpe, V.P. Ting, A. Noguera-Díaz, T.J. Mays, Isosteric enthalpies for hydrogen adsorbed on nanoporous materials at high pressures, Adsorption 20 (2) (2014) 373–384.
[62] P.A. Georgiev, D.K. Ross, A.D. Monte, U. Montaretto-Marullo, R.A.H. Edwards, A.J. Ramirez-Cuesta, D. Colognesi, Hydrogen site occupancies in single-walled carbon nanotubes studied by inelastic neutron scattering, J. Phys. Condens. Matter 16 (8) (2004) L73.
[63] R.J. Olsen, A.K. Gillespie, C.I. Contescu, J.W. Taylor, P. Pfeifer, J.R. Morris, Phase transition of H2 in subnanometer pores observed at 75 K, ACS Nano 11 (11) (2017) 11617–11631.
[64] Jacek Jagiello, James Olivier, 2D-NLDFT adsorption models for carbon slit-shaped pores with surface energetical heterogeneity and geometrical corrugation, Carbon 55 (2013) 70–80, https://doi.org/10.1016/j.carbon.2012.12.011.